Available online at www.sciencedirect.com
SCIENCE DIRECT®
Journal of Computational Physics 198 (2004) 747–770
JOURNAL OF COMPUTATIONAL PHYSICS
www.elsevier.com/locate/jcp

Numerical simulation of the impact of liquid droplets on porous surfaces

Neyval C. Reis Jr. [a,*], Richard F. Griffiths [b], Jane M. Santos [a]

[a] *Departamento de Engenharia Ambiental, Universidade Federal do Espirito Santo, Av. Fernando Ferrari, s/n Goiabeiras, 29060-970 Vitoria, ES, Brazil*
[b] *Environmental Technology Centre, Department of Chemical Engineering, UMIST, PO Box 88, M60-1QD, UK*

Received 16 July 2003; received in revised form 17 December 2003; accepted 28 January 2004
Available online 27 February 2004

Abstract

This work presents a numerical model, based on the finite volume method, to study the dynamics of the impact/absorption of a liquid droplet impinging on a porous medium. To accurately represent the dynamics of the fluid flow special attention is given to the effects of surface tension and capillary forces, the movement of the free surface inside the porous medium, and the link between the fluid flow outside and inside the porous medium. The method of marker particles is used to track the position and the shape of the liquid region. The SIMPLEC algorithm is selected to solve the pressure–velocity coupling. In order to verify the accuracy of the proposed computational model, its predictions have been compared with data from a number of experimental studies dealing with various aspects of the overall behaviour. In general, the model shows a good level of agreement with these experimental data.

Keywords: Porous medium; Liquid droplets; Impact; Finite volume method

1. Introduction

Numerical and experimental investigations of the impact of liquid droplets on porous surfaces are important for a wide range of situations, varying from environmental applications to inkjet printing technology. A few studies have been specifically concerned with droplet impingement on permeable surfaces, among others [1–5]. Although these studies present detailed experimental investigations of the phenomenon, the experimental techniques that were used imposed serious limits on the amount of information obtained concerning the behaviour inside the porous substrate, as well as on the minimum time scale resolved. Thus, it is possible to analyse the influence of the governing parameters on the final shape of the impinged/absorbed droplet, but it is not possible by these methods to resolve the mechanisms while they are

* Corresponding author. Tel.: +27-33352177; fax: +27-33352648.
E-mail address: neyval@ambiental.ufes.br (N.C. Reis Jr.).

0021-9991/$ - see front matter © 2004 Published by Elsevier Inc.
doi:10.1016/j.jcp.2004.01.024

occurring. By contrast, a numerical investigation of the fluid flow dynamics during the impact/absorption phenomenon can resolve these mechanisms, and enable a better understanding of the process.

There is a substantial amount of work published in the literature about numerical models for the impact of liquid droplets upon solid surfaces. One of the first reported studies was performed by Harlow and Shannon [6], who used the "marker-and-cell" (MAC) finite-difference method to simulate a liquid droplet impact and deformation, neglecting the effects of viscosity and surface tension to simplify the problem. Subsequently, Tsurutani et al. [7] enhanced the MAC model to include surface tension and viscosity effects, improving considerably the accuracy of the simulations. Since then, numerous papers have been published reporting two-dimensional and three-dimensional [8–10] droplet impact simulations and the introduction of more refined numerical techniques to improve predictions, including the use of adaptative grids [11–13].

All models described above were mainly concerned with the impact of liquid droplets on a non-permeable surface. In spite of the importance of the numerical study of the impact of droplets on permeable surfaces for a wide range of applications, there appear to be no reported studies in the literature. Most of the studies on droplets absorption by porous media are based on the use of the viscous-controlled Lucas–Washburn absorption theory to predict the spread and absorption of the liquid by the porous substrate, such as [14,15]. More recently, Seveno et al. [16] combined the dynamics of spreading for sessile drops and the Lucas–Washburn equation to describe the dynamics of droplets spreading on a porous surface. However, these models did not include the inertial effects related to impact simulations, and were mostly focused on the spontaneous spreading of droplets resting on porous surfaces.

The work reported here presents a numerical model to study the dynamics of the impact/absorption of a liquid droplet on a porous medium. As depicted in Fig. 1, this problem addresses a more complicated set of physical phenomena than impingement on non-permeable surfaces, since at the same time that the axial momentum of the droplet is transformed to radial momentum, the pressure at the impact point also forces the liquid to move through the permeable surface and into the substrate. Furthermore, capillary effects and wettability tend to draw the liquid into the porous substrate.

Accordingly, there are three main issues that need to be addressed in order to obtain a mathematical description of the phenomenon: (i) the fluid flow outside and inside the porous medium, (ii) the flow through the atmosphere/porous medium interface, and (iii) the treatment of the free surface of the liquid droplet. In order to represent these features accurately, an algorithm based on the finite volume technique [17] and the marker-particle technique [18] is presented, including the effects of surface tension inside and outside the porous medium, as well as the drag imposed by the solid particles in the porous substrate. In order to verify the accuracy of the computational model, comparisons were made with data from previous

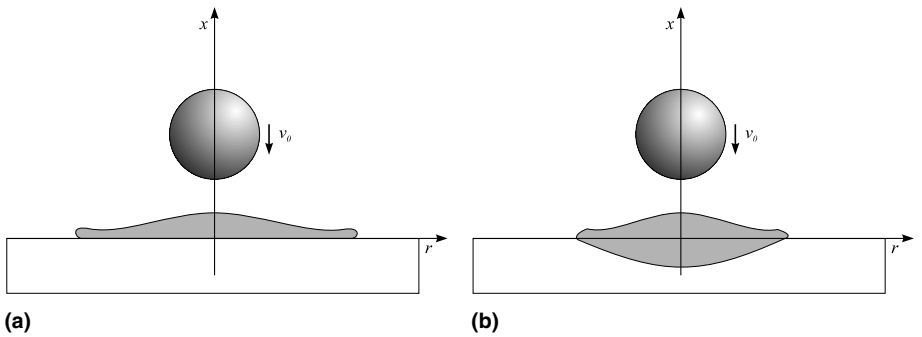

Fig. 1. Schematic representation of the droplet impingement problem: (a) impingement on a non-permeable flat surface and (b) impingement on a permeable flat surface.

experimental work [4,5,19–21], including photographic records of droplet behaviour during impact, measured values of the droplet spread ratio, and Nuclear Magnetic Resonance (NMR) images of the liquid within the porous substrate.

2. Mathematical modelling

The fluid flow described above represents a typical case of a free surface flow. Fluid flows are classified as free surface flows when a fluid has one or more boundaries in the form of interfaces with another fluid and the external fluid has a negligible influence on the motion of the internal fluid [6,7,10–13]. This assumption is valid, typically, in situations where the viscosity and density of the internal fluid are much larger than the viscosity and density of the external fluid.

Free surface flows represent a particular case of two-phase flows. An extension of a free surface flow computational method to a two-phase flow calculation would not represent a significant increase in complexity, if the same equations were applied to both phases and solved along with the full boundary conditions at the interface. However, when the influence of the external fluid is negligible, it is more cost-effective to solve a single-phase problem and neglect the effects of the external fluid.

In this work, the calculations start at the moment that the droplet comes in contact with the porous surface. From this instant, the influence of the external fluid (atmosphere) can be neglected, in accordance with the basic assumption of a free surface flow. Under these conditions, viscous stress at the free surface interface can be neglected, making the tangential stress equal to zero at the free surface and the normal stress determined by surface tension, curvature and outer pressure.

The fluid flow in the core of the liquid droplet is governed by the momentum conservation and continuity equations, both outside the porous medium and inside the microscopic pores of the porous medium. Momentum and continuity equations could be used throughout both regions, as long as the shape and dimensions of each particle of the porous substrate are accounted for when the shape of the computational domain is defined. Obviously, this approach is far from practical, due to the complexity of the porous network and the number of particles forming a porous material.

It is therefore necessary to change from a microscopic field of view, where continuity and momentum equations are valid and the porous network is rather chaotic, to a macroscopic field of view, where the effects of the porous network can be treated as averaged quantities. As a consequence, the governing equations of the fluid flow inside the porous substrate are slightly different from the usual momentum and continuity equations, since they have to account for the averaged effects of the porous substrate on the fluid flow, namely viscous friction and the pressure drag of the solid matrix.

Although each region of the fluid flow is governed by a different set of equations, it is important to note that momentum matching conditions at the interface between the two regions must be observed, since both sets of equations must express the overall momentum conservation. In the following sections the fundamental equations governing the phenomenon are presented, along with the treatment of the free surface of the fluid inside and outside the porous substrate.

2.1. Co-ordinate definition

Before introducing the fundamental equations governing the phenomenon, it is important to define the co-ordinate system and the mathematical notation used. In view of the symmetrical nature of the problem, governing equations are written in cylindrical co-ordinates and in the axi-symmetric form. Accordingly, the problem is described in a two-dimensional form, where x and r are the axial and radial co-ordinates, respectively, as shown in Fig. 2.

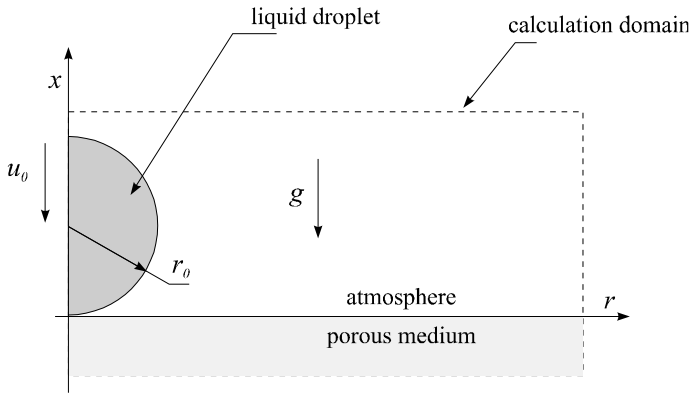

Fig. 2. Co-ordinate system in the computational domain.

2.2. Governing equations outside the porous medium

As explained above, the fluid flow is governed by the continuity of mass and momentum conservation equations. The equations for constant density (ρ) and viscosity (μ) are given by

$$\nabla \cdot \mathbf{u} = 0, \tag{1}$$

$$\rho\left[\frac{\partial \mathbf{u}}{\partial t} + \mathbf{u} \cdot \nabla \mathbf{u}\right] = \nabla \boldsymbol{\sigma} + \rho \mathbf{g}, \tag{2}$$

where $\mathbf{u}$ is the velocity vector, p is the pressure, $\mathbf{g}$ is the acceleration due to gravity and $\boldsymbol{\sigma}$ is the stress tensor, which can be written for a Newtonian fluid as

$$\boldsymbol{\sigma} = -p\mathbf{I} + 2\mu\nabla\mathbf{u}. \tag{3}$$

2.2.1. Treatment of the free surface

At the free surface the influence of the viscous stress due to the action of the external fluid is negligible. Thus, the tangential stress at the free surface is zero, and the normal stress is determined by surface tension, curvature and outer pressure. Therefore, the normal stress at the free surface can be described as

$$\boldsymbol{\sigma}_{\mathbf{n}} = -p_s\mathbf{n}, \tag{4}$$

where p_s is the pressure at the interface, or surface pressure, and $\mathbf{n}$ is the unit vector normal to the fluid interface, whose components are n_x and n_r.

The surface pressure (p_s) is given by the sum of the external pressure and the pressure jump due to surface tension. For incompressible fluid flows, the outer pressure is often assumed to be constant and thus does not influence the flow. Thus, it is possible to re-write the stress tensor at the free surface as

$$\boldsymbol{\sigma}_{\mathbf{n}} = -(2\gamma\kappa)\mathbf{n}, \tag{5}$$

where κ is the mean surface curvature and γ is the surface tension coefficient of the liquid.

2.2.2. Curvature radius and slope of the free surface

As already noted, the fluid velocity at each point of the liquid region is used to account for movement and deformation of the fluid interface, tracking the free surface shape and location throughout the cal-

culation. This procedure is described fully in Section 3. As the position of the free surface is known during the calculations, the slope and orientation of the fluid interface can be used to determine the mean surface curvature (κ) and the direction of the vector normal to the fluid interface (**n**).

The first step is to define an appropriate co-ordinate system to account for the free surface deformation. As shown in Fig. 3, the position of the interface is used to define an additional co-ordinate s [22], which is measured along the free surface. Each point of the fluid interface has its position mapped by a function of s, where $x_1(s)$ indicates the position along the co-ordinate axis r for each point in s, and $x_2(s)$ indicates the position along the co-ordinate axis x for each point in s

$$x_1(s) = r, \quad x_2(s) = x. \tag{6}$$

The components of the vector normal to the interface are given by

$$n_r = -x_2', \quad n_x = x_1', \tag{7}$$

where the primed quantities indicate differentiation with respect to s ($x_i' = \mathrm{d}[x_i'(s)]/\mathrm{d}s$). For the axi-symmetric configuration employed it can be shown that [22]

$$\kappa = \frac{x_1^2(x_2''x_1' - x_1''x_2') + [(x_1')^2 + (x_2')^2]x_1x_2'}{2x_1^2\left[(x_1')^2 + (x_2')^2\right]^{3/2}}. \tag{8}$$

The wetting effect is usually modelled through the contact angle (θ) between the solid surface and the liquid interface. Thus, at the contact line

$$x_1' = -\cos\theta, \quad x_2' = \sin\theta. \tag{9}$$

By introducing the values of these derivatives on the interpolation functions used to describe $x_1(s)$ and $x_2(s)$ (which are discussed in Section 3), it is possible to determine the values of x_1, x_2, x_1'' and x_2'' at the contact line, and determine the mean curvature by using Eq. 8.

The contact angle value used in the expressions above is the dynamic contact angle. Scriven [23], and more recently Gennes [24] presented a comprehensive review of the theory of the dynamics of the fluid interface and contact angle. The main aspect that should be considered when modelling the fluid/solid

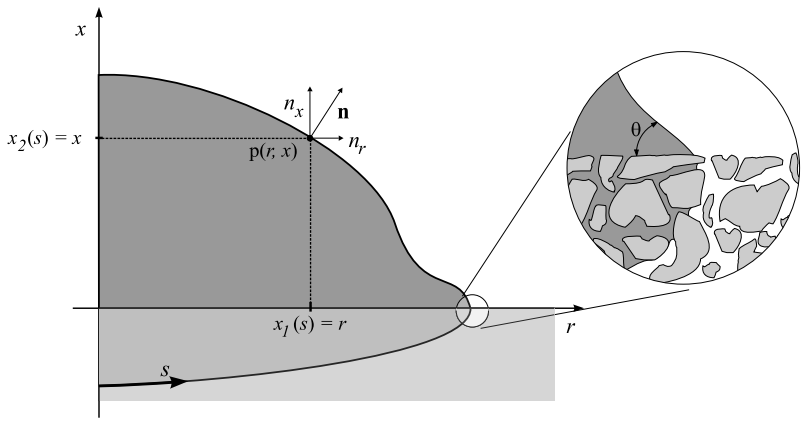

Fig. 3. Co-ordinate definition.

interface is that the dynamic contact angle for spreading is significantly larger than the dynamic contact angle for recoiling.

Fukai et al. [22] propose that the variation of the contact angle can be accounted for in the mathematical description of the problem by the specification of different values of the contact angle θ if the contact line is advancing or recoiling. Although this approach does over-simplify the problem, since it is known that the dynamic contact angle actually depends on the velocity of the contact line, the numerical simulations of droplets impinging on solid surfaces obtained with this method are in very close agreement with experimental observations. The accuracy of this hypothesis is mainly related to the fact that the influence of the velocity of the contact line on the dynamic contact angle is more pronounced at very low velocities (of the order of mm/s or less, according to [25]). By contrast, the velocity of the contact line in impingement droplet studies can reach values higher than the impinging velocity, which is of the order of m/s, and it is maintained at this level during the greater part of the spreading episode. Therefore, in the present work the approach proposed by [22] is used to describe the dynamic contact angle.

2.3. Governing equations inside the porous medium

As outlined previously, the theoretical formulation of momentum and mass transfer in porous media is usually obtained by a change from the microscopic scale, where the representative volume is small in comparison to the pore dimensions, to a macroscopic scale, where the size of the representative volume is large compared to the pore dimensions. Whitaker [26], and more recently Hsu and Cheng [27], presented a formal derivation of the general equation for fluid flow through a rigid and homogeneous porous medium. This approach is based on a volume averaging of the microscopic conservation equations over a representative volume, yielding the macroscopic form of the mass and momentum conservation equations in the porous medium

$$\overline{\nabla} \cdot \mathbf{u}_\mathrm{p} = 0, \tag{10}$$

$$\rho\left[\frac{\partial \mathbf{u}_\mathrm{p}}{\partial t} + \mathbf{u}_\mathbf{p} \cdot \overline{\nabla}\frac{\mathbf{u}_\mathrm{p}}{\epsilon}\right] = \overline{\nabla}\boldsymbol{\sigma}_\mathrm{p} + \mathbf{B} + \rho\mathbf{g}\epsilon, \tag{11}$$

where $\mathbf{u}_\mathrm{p}$ is the Darcy velocity vector, also called the macroscopic averaged velocity vector in the porous medium, ϵ is the porosity of the medium and p_p is the macroscopic averaged pressure. $\overline{\nabla}$ denotes the macroscopic gradient operator [27]. $\boldsymbol{\sigma}_\mathrm{p}$ is the macroscopic stress tensor calculated using the macroscopic averaged velocity ($\mathbf{u}_\mathrm{p}$) and the macroscopic averaged pressure (p_p)

$$\boldsymbol{\sigma}_\mathrm{p} = -p_\mathrm{p}\mathbf{I} + 2\mu\overline{\nabla}\mathbf{u}_\mathrm{p}. \tag{12}$$

According to the averaging procedure the value $\mathbf{u}_\mathrm{p}$ denotes the product of the fluid velocity ($\mathbf{u}$) by the porosity (ϵ), i.e., $\mathbf{u}_\mathrm{p} = \epsilon\mathbf{u}$. Similarly, the value of p_p represents the product of the pressure (p) by the porosity (ϵ), i.e., $p_\mathrm{p} = \epsilon p$ [27].

$\mathbf{B}$ is the total drag force per unit volume (body force) due to the presence of the solid particles, which represents the sum of the pressure drag and viscous friction. In the present work Ergun's correlation [28] is used to express total drag force, which can be written as

$$\mathbf{B} = -\left[\frac{\mu\epsilon\mathbf{u}_\mathrm{p}}{K} + \rho\frac{F_\mathrm{p}\epsilon\mathbf{u}_\mathrm{p}|\mathbf{u}_\mathrm{p}|}{\sqrt{K}}\right], \tag{13}$$

where K and F_p are the permeability and the inertia factor. For a randomly packed bed of spheres such coefficients can be expressed in terms of the porosity (ϵ) and the diameter of the particles in the porous medium (d_p) as

$$K = \frac{\epsilon^2 d_p^2}{c_1(1-\epsilon)^2}, \quad F_p = \frac{c_2}{\sqrt{c_1}\epsilon^{3/2}}, \tag{14}$$

where c_1 and c_2 are empirical constants ($c_1 = 150$ and $c_2 = 1.75$). These relationships have been extensively validated and utilised to model fluid flows through porous substrates, among others [27,29,30].

2.3.1. Treatment of the free surface

The treatment given to the free surface outside the porous medium should also be applied to the free surface inside. However, in contrast with the macroscopic curvature radius of a free surface outside a porous medium, the liquid inside the porous medium is restricted by the dimensions of the capillaries, as shown in Fig. 4. Therefore, inside the porous medium the macroscopic mean curvature radius is no longer important; instead, the microscopic curvature radius inside the capillaries is the important parameter in the force balance. By analogy with the situation outside the porous medium, where the macroscopic curvature radius is responsible for a surface pressure, the meniscus formed in the liquid front inside a capillary is responsible for a surface pressure, which is called capillary pressure. This capillary pressure is extremely dependent on the porous medium structure, since the surface tension force acting on the liquid front is directly related to the dimensions of the capillaries.

Therefore, outside the porous medium the surface pressure is calculated as a function of the macroscopic curvature radius (Eq. (8)), and inside the porous medium the surface pressure is set as the capillary pressure value for a fully saturated medium. Thus, the normal component of the stress tensor on the free surface is expressed as

$$\boldsymbol{\sigma}_n = -p_s \mathbf{n} \begin{cases} \text{inside the porous medium} \rightarrow p_s = \epsilon p_c, \\ \text{outside the porous medium} \rightarrow p_s = 2\gamma\kappa. \end{cases} \tag{15}$$

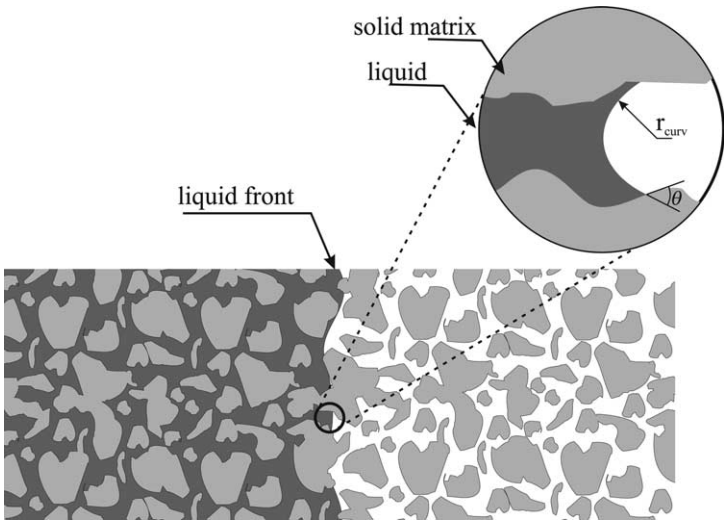

Fig. 4. Representation of a liquid front inside a porous medium, where r_{curv} is the curvature radius and θ is the contact angle.

In order to calculate the value of $\boldsymbol{\sigma}_n$ inside the porous medium, it is necessary to determine the direction of the unit vector normal to the free surface and the value of the capillary pressure. The same procedure used to calculate the vector normal to the free surface outside the porous medium is used to calculate it inside the porous medium. However, due to the different nature of the capillary pressure inside the porous substrate, further discussion is necessary to achieve a satisfactory formulation for its value.

2.3.2. Capillary pressure

Fig. 4 depicts the liquid inside the porous medium. In this region the capillary pressure depends on the dimensions of the capillaries and the contact angle between the liquid and solid particles. Accordingly, the capillary pressure can be written as [31]

$$p_c = -\frac{4\gamma\cos\theta}{d_{pores}}, \tag{16}$$

where d_{pores} is the diameter of the capillary, γ is the surface tension coefficient and θ is the contact angle at the solid/liquid interface.

If the contact angle is less than 90°, the meniscus formed inside a capillary will be concave as seen from the empty pore space. Capillary pressure will then have a negative value, which creates a pressure differential resulting in wetting of the porous medium, i.e. the capillary pressure will tend to pull the liquid front into the porous substrate. On the other hand, if the contact angle is larger than 90°, the meniscus will be convex and the capillary pressure will be positive, i.e. capillary pressure will oppose the propagation of liquid into the porous medium. In this case, the liquid will have to overcome this resistance in order to propagate inside the porous substrate.

The porous substrate has so far been characterised by using the value of porosity (ϵ) and the particle diameter of the medium (d_p). Eq. (16) adds one more parameter to this characterisation, namely the pore diameter d_{pores}.

For a wide range of situations the value of d_{pores}/d_p is approximately constant, such as for sand, glass beads and some ceramic materials where the assumption of a perfectly packed bed of spheres is valid. Therefore, it is convenient to re-write Eq. (16) as

$$p_c = -\frac{4\gamma\cos\theta}{\alpha d_p}, \tag{17}$$

where

$$\alpha = \frac{d_{pores}}{d_p}. \tag{18}$$

Before closing the discussion on the capillary pressure value, it is important to note that although the discussions here are focused on the average pore size in the porous substrate, there is a distribution of pore sizes around the mean value. Accordingly, the capillary pressure also depends on the level of saturation (or concentration of liquid) in the porous medium. In this work the liquid front inside the porous medium is treated as a sharp front, i.e. inside the region occupied by the liquid the porous medium is fully saturated and outside the region occupied by liquid the saturation level is negligible. This approach simplifies the problem, since it is not necessary to deal with the variation of the capillary pressure as a function of the saturation level. In practice, however, instead of a sharp interface there is a gradient separating the saturated and non-saturated regions of the porous medium, due to the effects of capillary diffusion. The approach described above limits the ability of the model to predict the capillary diffusion, since its main mechanism is related to the variation of the capillary pressure with saturation levels [31–33]. However, as discussed by Reis et al. [5], the time scale of the capillary diffusion is far greater than the time scale of the

droplet impingement and absorption, which makes this transport mechanism negligible over the time frame of droplet impingement.

2.4. Linking the external and the internal fluid flows

After determining the form of the governing equations of the phenomenon, it is necessary to link the equations for the fluid flow outside and inside the porous medium. The equations governing the external and internal flows must obey the matching conditions at the porous medium interface.

These conditions express continuity of normal and tangential velocities, pressure, and the normal and shear stresses. The boundary conditions at the interface can be summarised as [30]

$$\mathbf{u} = \mathbf{u}_{\mathrm{p}}, \quad p = p_{\mathrm{p}}, \quad \frac{\partial \mathbf{u}}{\partial x} = \frac{\partial \mathbf{u}_{\mathrm{p}}}{\partial x}, \tag{19}$$

where x is the direction normal to the surface of the porous medium. If these conditions are observed, there is momentum conservation across the interface, and the results obtained are free from discontinuities.

It should be noted that the equations governing external and internal flows (Eqs. (2) and (11)) are very similar. The main differences are in the term dealing with the drag of the solid matrix and the appearance of the porosity value in the inertia term of the momentum equation inside the porous medium. Due to this similarity, Hadin [29] proposed that instead of solving the two sets of governing equations separately, the equations can be combined into one set. In this approach, the continuity and momentum equations (Eqs. (1) and (2)) for the fluid flow are solved throughout the computational domain and the additional terms required in the governing equations for the porous medium (Eq. (11)) are added to the ordinary momentum equation (Eq. (2)) inside the domain region occupied by the porous matrix. With this procedure, the velocity vectors obtained outside the porous medium represent the fluid velocities, while inside the porous medium the velocity vectors represents the macroscopic averaged velocities ($\mathbf{u}_{\mathrm{p}}$). This ensures that the matching conditions at the surface of the porous medium are automatically satisfied and the numerical solution algorithm is greatly simplified.

3. Numerical method

Having described the governing equations, the next step is to introduce the solution method. The main contribution of this work is related to the treatment of the free-surface and the fluid representation. The numerical techniques used to solve the mass and momentum conservation equations are standard well-known techniques described elsewhere [17,34]. Accordingly, this account is mainly focussed on the treatment of the free-surface and only a short description of the numerical methods used to solve the conservation equations is given.

The governing equations are discretised using the finite volume method [17], on a fixed orthogonal grid, whose geometry is defined according to Fig. 5. The transport equations are solved only for the region occupied by the liquid, and the free-surface boundary conditions are applied at the interface between the atmosphere and the liquid region. A staggered grid is used for the velocity components, while the scalar variables are stored at the nodal point at the centre of each of the control volumes. The power-law differencing scheme [17] is used in the integration of convective/diffusive terms. In order to avoid the diffusive constraint on the time step size, a fully implicit integration scheme was used in the present work. The pressure–velocity coupling problem is solved by using the SIMPLEC (SIMPLE – Consistent) algorithm, where the continuity equation is used to derive a discretised equation describing the pressure field [35].

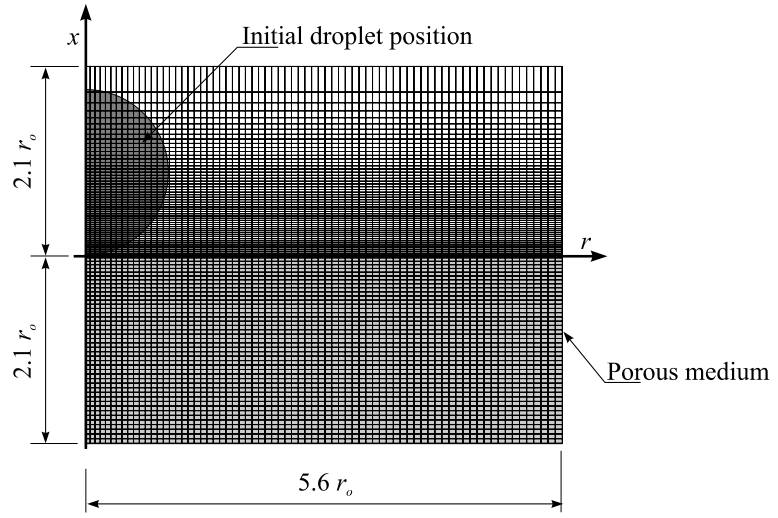

Fig. 5. Schematic representation of the grid used for the simulations, where r_0 denotes the initial radius of the droplet.

The marker-particle method is used to track the position and the shape of the liquid region. Despite the increase of memory usage by comparison with the VOF method [36], the marker-particle method is chosen in view of its simple implementation and easy expansion to three-dimensional situations if needed. The marker-particle method tracks the position of the fluid through the use of virtual massless particles, which represent the region occupied by the liquid. These particles serve to show the motion of the fluid and its deformation through the computational domain and to indicate the correct location of the interface, where the free surface boundary conditions should be applied. The marker particles do not have any influence in the fluid flow calculation. They serve only to indicate the shape and position of the fluid region, determining which cells are full cells (cells containing fluid), empty cells or surface cells (cells containing the interface). Within this classification, the transport equations are solved only for the region occupied by the liquid (full cells), and the free surface boundary conditions are applied at the interface (surface cells).

As the marker particles are used to indicate the shape and position of the fluid region, it is necessary to move the marker particles at each time step interval. Therefore, the calculation scheme is divided into two stages at each time step. First, the governing flow equations are solved for the cells containing particles, and the velocity field in the liquid is determined. Then each particle is moved according to the liquid velocity at its position.

The key points of a correct representation of a free surface fluid flow are the particle movement technique and the correct implementation of the boundary conditions at the free surface. The next two sections are devoted to these topics.

3.1. Particle movement

In order to move the marker particles, it is necessary to determine the fluid velocity at the marker positions. As the finite volume solution is discrete, i.e. the solution is known only at discrete points throughout the computational domain, it is necessary to interpolate the velocities calculated at the nodal points to the particle position. The particle velocity components (u_{part}, v_{part}) are calculated using bilinear interpolation of the velocity values at the nearest four nodal points, and the new particle positions after a time interval Δt are obtained from the Taylor series considering only the first order term

$$x(t+\Delta t) = x(t)_{\text{part}} + u(t)_{\text{part}}\Delta t,$$
$$r(t+\Delta t) = r(t)_{\text{part}} + v(t)_{\text{part}}\Delta t, \tag{20}$$

where $x(t)_{\text{part}}$ and $r(t)_{\text{part}}$ denote the position of the particle at the instant t, $x(t+\Delta t)_{\text{part}}$ and $r(t+\Delta t)_{\text{part}}$ denote the position of the particle at the instant $t+\Delta t$, $u(t)_{\text{part}}$ and $v(t)_{\text{part}}$ denote the particle velocity components obtained from the interpolation of the four nearest nodal points.

It is important to note that inside the porous medium the momentum equation is written in terms of the Darcy velocity ($\mathbf{u}_{\text{p}}$). In order to maintain physical consistency and ensure mass conservation, the particles inside the porous medium must be moved with the fluid velocity ($\mathbf{u}$) instead of the Darcy velocity ($\mathbf{u}_{\text{p}}$). If the particle velocity is calculated based on the value of the four nearest neighbours, its value will be relative to $\mathbf{u}_{\text{p}}$. Thus, in order to ensure mass conservation inside the porous medium

$$x(t+\Delta t) = x(t)_{\text{part}} + \frac{1}{\epsilon}u(t)^{\text{p}}_{\text{part}}\Delta t,$$
$$r(t+\Delta t) = r(t)_{\text{part}} + \frac{1}{\epsilon}v(t)^{\text{p}}_{\text{part}}\Delta t, \tag{21}$$

where $u(t)^{\text{p}}_{\text{part}}$ and $v(t)^{\text{p}}_{\text{part}}$ denote the particle velocity components obtained from the interpolation of the four nearest nodal points inside the porous medium, and ϵ represents the porosity value. This correction is necessary due to the volume averaging approach used to derive the momentum equations inside the porous medium [26,27]. Based on this approach each control volume inside the porous medium is partially occupied by liquid and partially occupied by the solid matrix of the substrate. Therefore, the Darcy velocity ($\mathbf{u}_{\text{p}}$) represents the velocity vector averaged on a representative macroscopic volume (see [27] for details), expressing contributions of the fluid flow and motionless solid matrix of the substrate. Thus, the actual fluid velocity inside the porous medium is in fact represented by $\mathbf{u}$ or $\mathbf{u}_{\text{p}}/\epsilon$.

3.2. Implementation of the free surface boundary conditions

In addition to the particle movement procedure, a free surface fluid flow description must account correctly for the boundary conditions at the free surface. As explained in the previous section, at the free surface the influence of the viscous stress due to the action of the external fluid is negligible, and the normal stress is determined by surface tension and pressure gradients due to the external pressure.

Therefore, if the cells containing the free surface are considered to be inviscid [6,34,36], the viscous term of the stress tensor vanishes, and the stress at the free surface is determined only as a function of the surface pressure. In order to ensure that

$$\boldsymbol{\sigma}_{\text{n}} = -p_{\text{s}}\mathbf{n} \tag{22}$$

the value of the pressure at each discretisation cell containing the free surface (surface cell) is set to the surface pressure value (p_{s}). If the free surface is inside the porous medium, the surface pressure is the capillary pressure (p_{c}). If the free surface is outside the porous medium the surface pressure is the pressure due the macroscopic curvature radius (κ). In addition, the pressure gradient term in the discretised momentum equation for each direction is multiplied by the component of the vector normal to the free surface at each surface cell.

In order to implement these modifications, it is necessary to have knowledge of the slope and curvature of the free surface, which are required to determine the pressure gradient term along the free surface and the surface pressure due to surface tension outside the porous medium.

3.2.1. Curvature radius and slope of the free surface

Although marker particles are used to indicate the shape of the region occupied by fluid during the calculations, it is very difficult to quantify the slope and curvature of the free surface, since there is no clear distinction between particles close to the surface and those in the core of the liquid. Therefore, in order to indicate precisely the shape of the free surface and to determine its curvature radius and slope, an additional set of particles is used, which are known as interface particles [37]. As shown in Fig. 6, these particles are initially placed in order along the free surface and thereafter are moved using the fluid velocities, as for any other marker particles, so that as the calculation proceeds the location of these particles indicates the shape of the free surface. Accordingly, their position can be used to generate an interpolation function describing the position of the free surface, and by using Eqs. (7) and (8), it is possible to determine the components of the vector normal to the free surface and the curvature radius (κ).

In the present work, two second order polynomial functions are used to describe the shape of the free surface. The first expresses the variation of the position of the free surface in the r co-ordinate as a function of the s co-ordinate, and the second expresses the variation of the position of the free surface in the x co-ordinate as a function of the s co-ordinate. The position (r,x) of the free surface is then written as

$$(r,x) = (x_1(s), x_2(s)), \tag{23}$$

where $x_1(s)$ is the second order Lagrange polynomial describing r and $x_2(s)$ is the second order Lagrange polynomial describing x. During the calculations of the surface pressure and normal vector for each control volume containing the free surface (surface cell), the interpolating polynomials are calculated based on the (r,x) position of the three nearest interface particles.

In order to account for contact angle between the liquid outside the porous medium and the surface of the porous medium (θ), an additional interface particle was added (as shown in Fig. 6). This particle was positioned at the interface of between the atmosphere and the porous medium and its radial position was calculated so that the shape of the surface of liquid outside the porous medium would present the correct contact angle with the surface of the substrate.

The values calculated by Eqs. (7) and (8) represent point values of the surface curvature and normal vector, which can vary strongly along the free surface. In order to determine the mean values of curvature

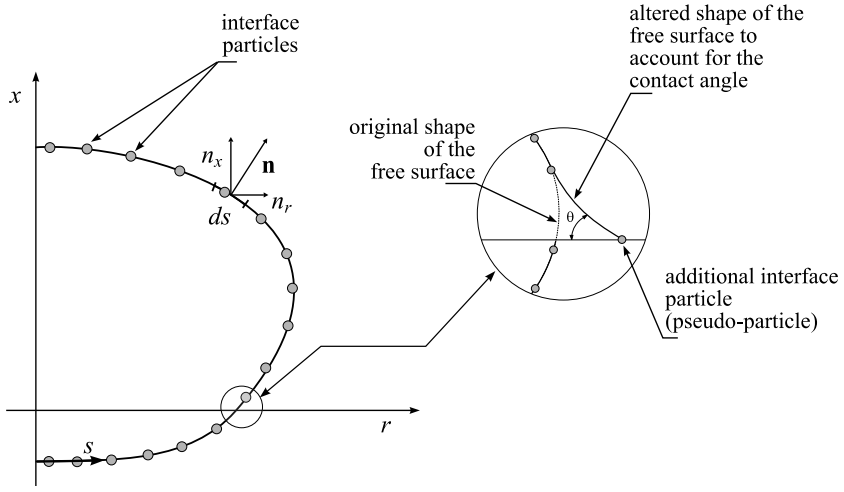

Fig. 6. Schematic representation of the interface particles.

and slope of the free surface inside a control volume (calculation cell), the point values are numerically integrated over the s co-ordinate along the segment of the free surface inside the control volume:

$$\overline{n_r} = \frac{1}{(S_2 - S_1)} \int_{S_1}^{S_2} -x_2' \, \mathrm{d}s, \tag{24}$$

$$\overline{n_x} = \frac{1}{(S_2 - S_1)} \int_{S_1}^{S_2} x_1' \, \mathrm{d}s, \tag{25}$$

$$\overline{\kappa} = \frac{1}{(S_2 - S_1)} \int_{S_1}^{S_2} \kappa \, \mathrm{d}s, \tag{26}$$

where S_1 and S_2 are the points where the free surface intersects the control volume boundaries, as shown in Fig. 7.

3.3. Determination of the surface velocity

In the solution procedure the pressure correction algorithm (SIMPLEC) ensures mass conservation at each control volume of the computational domain. However, since pressure correction is omitted in the surface cells, as pressure is set to a fixed value, it is necessary to enforce mass conservation individually at each surface cell. In order to accomplish this, it is necessary to ensure that the velocity of the free surface moving inside a control volume is based on the amount of mass entering or leaving this control volume. The specification of these values in the present work is the same as that commonly used in earlier MAC methods. The velocities immediately outside the surface represent the surface velocity, and are defined as the velocity between a surface cell and its adjacent empty neighbour. These velocities are calculated by the continuity equation, in order to ensure the conservation of mass in the surface cells. However, if a surface cell has two or more neighbouring empty cells, there are too many unknown velocities, and there is not enough information to use the continuity equation. Thus, the individual terms of the continuity equation should be separately set to zero. A complete description of the procedure used to determine the surface velocity is given by Reis [38].

It should be noted that if mass conservation is guaranteed in all control volumes, the total mass flux in the domain must be zero, i.e. for an incompressible fluid, if the free surface is expanding in one direction, it

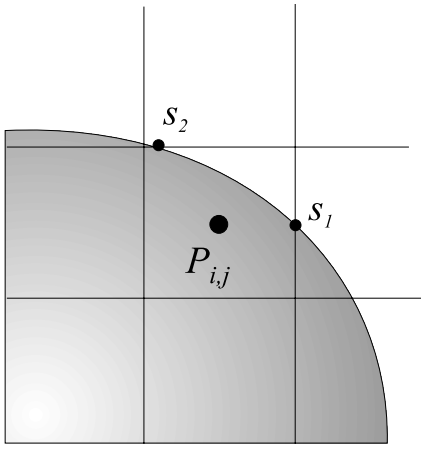

Fig. 7. Schematic representation of the points (S_1 and S_2) where the free surface intersects the control volume boundaries.

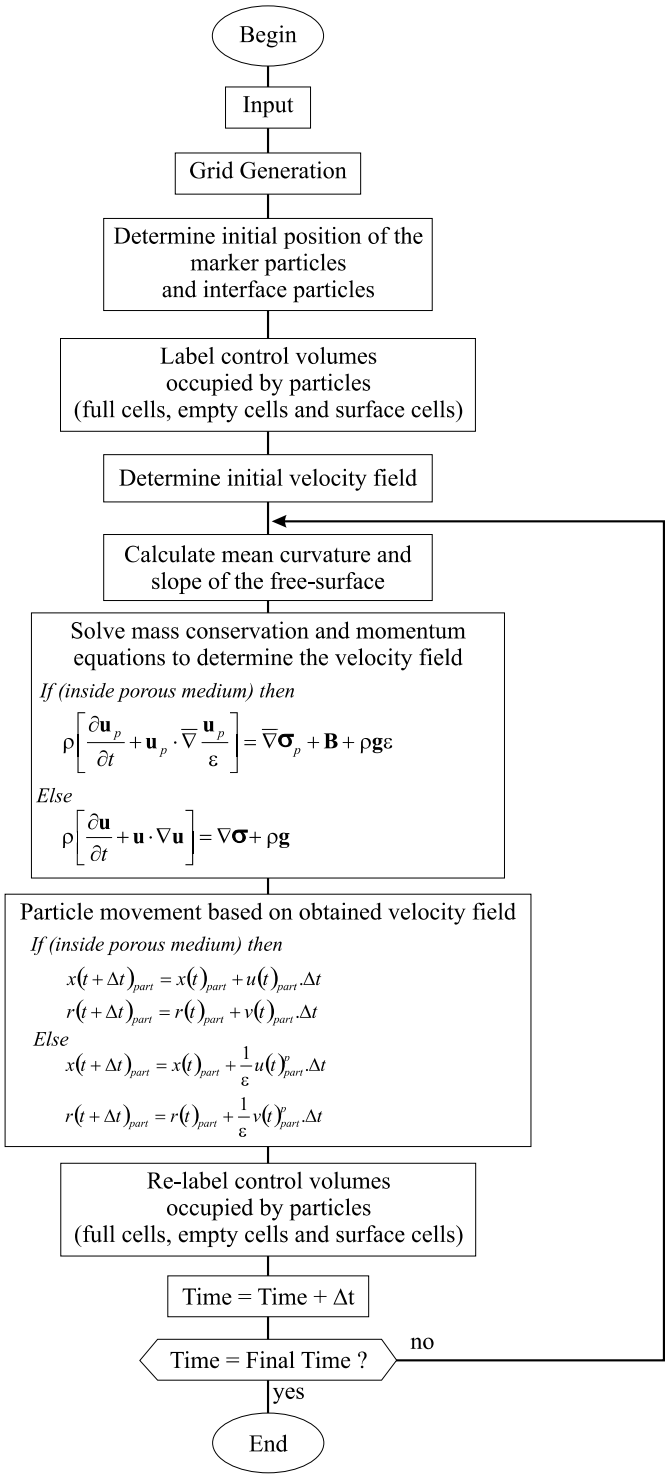

Fig. 8. Schematic representation of the global structure of the solution algorithm.

should be retracting in another direction to satisfy the volume conservation of the liquid. This provides a continuous check of the consistency of the solution throughout the calculation.

3.4. Computational procedure

The computational procedure was implemented in FORTRAN 90. Fig. 8 presents a global view of the solution algorithms, which involves the grid generation, initial particle positioning, labelling control volumes, solution of the fluid dynamics equations and particle movement.

4. Results and model validation

In this section the results obtained by numerical simulation are presented and the accuracy of the model is discussed. The main features of the phenomenon are discussed, but emphasis is given to the validation of the model.

In order to verify the accuracy of the computational model, the results obtained by numerical simulation are compared with experimental data. Four sets of experimental data available in the literature were selected for comparison, from [4,19–21]. These datasets include photographs of the impact/absorption dynamics [4], measurements of final spread ratio of droplets liquid droplets [19,20] and images of liquid droplets embedded in porous substrates just after impact, obtained by Nuclear Magnetic Resonance [21].

Tables 1 and 2 summarise the data used for comparison. It is important to note that the values of the main governing parameters vary over several orders of magnitude, exploring a wide range of situations. The dataset includes droplets of water, glycerol, *n*-heptane, diethyl-malonate (DEM) and methyl-salicylate (MES) impinging on ceramic, sand, concrete, and beds of glass beads. Cases 1, 2, 3, 6 and 7 correspond to the impingement of a liquid droplet on a consolidated porous medium, while the rest of the cases are for unconsolidated porous media.

In order to enable an easier parameterisation of the results, and the extrapolation of the data obtained to a wider range of physical situations, it is important to define non-dimensional variables to characterise the droplet shape and its time evolution. Thus, the following dimensionless variables are introduced:

$$R^* = \frac{r_{\text{droplet}}(t)}{r_0}, \quad H^* = \frac{h_{\text{droplet}}(t)}{r_0}, \quad Th^* = \frac{th_{\text{droplet}}(t)}{r_0}. \tag{27}$$

As indicated in Fig. 9, R^* is non-dimensional droplet radius (also knows as spread ratio), H^* is the non-dimensional penetration depth and Th^* is the non-dimensional thickness of the liquid layer outside the porous substrate. In addition, a non-dimensional time (t^*) is also defined

$$t^* = \frac{t}{r_0/u_0}. \tag{28}$$

Grid and time step size sensitivity tests were performed to determine the optimum grid and time step size. A numerical grid of 150×100 nodal points ($x \times r$) and a non-dimensional time step size (Δt^*) equal to 2.0×10^{-4} were selected for all numerical simulations presented.

Fig. 10 shows the comparison of the time evolution of the shape of the liquid droplet during impact obtained by numerical simulation and the photographs obtained by Chandra and Avedisian [4] (case 1). Obviously, the photographs present the image of the portion of the liquid droplet outside the porous substrate, while the numerical simulations display the liquid both inside and outside the porous region. The photographs represent a perspective view of the droplet, since the camera was positioned at a small angle in relation to the surface.

Table 1
Summary of the data used for comparison

Case	Substrate/liquid	V_0 (m/s)	r_0 (mm)	ϵ	K (m^2)	Dp (10^{-4} m)	α
1	Ceramic/*n*-heptane	0.930	0.750	0.25	1.04×10^{-12}	0.750	0.447
2	Concrete/DEM	3.694	1.815	0.12	1.00×10^{-14}	0.259	0.040
3	Concrete/MES	4.045	1.815	0.12	1.00×10^{-14}	0.259	0.040
4	Sand/DEM	3.694	1.815	0.37	8.51×10^{-12}	1.000	0.447
5	Sand/MES	4.045	1.815	0.37	8.51×10^{-12}	1.000	0.447
6	Concrete/DEM	1.694	0.685	0.12	1.00×10^{-14}	0.259	0.040
7	Concrete/DEM	1.494	2.030	0.12	1.00×10^{-14}	0.259	0.040
8	Sand/DEM	1.694	0.685	0.37	8.51×10^{-12}	1.000	0.447
9	Sand/DEM	1.494	2.030	0.37	8.51×10^{-12}	1.000	0.447
10	Sand/water	0.520	1.825	0.47	7.98×10^{-11}	1.800	0.447
11	Sand/glycerol	0.520	1.715	0.47	7.98×10^{-11}	1.800	0.447
12	Glass beads/water	0.520	1.660	0.45	2.89×10^{-11}	1.200	0.447
13	Glass beads/water	0.520	1.660	0.45	5.02×10^{-12}	0.500	0.447
14	Glass beads/water	0.520	1.660	0.45	3.21×10^{-10}	4.000	0.447

Case 1 is taken from[4], cases 2–5 are from [19], cases 6–9 are from [20] and cases 10–14 are from [21]. Concrete properties were based on [39,40], for Portland concrete. The value of θ for case 1 was taken from measurements performed by [4]. As for the other cases, there was no available data on θ for the liquids and the substrates used. Since the results obtained by the model did not present significant variation for contact angles ranging from 0° to 60°, droplets were considered to be perfectly wetting due to the lack of data.

Table 2
Summary of the liquid properties of the data used for comparison

Liquid	ρ (kg/m^3)	μ (Pa s)	γ (N/m)
n-Heptane	667.5	4.05×10^{-4}	2.01×10^{-2}
DEM	1055	4.00×10^{-3}	3.23×10^{-2}
MES	1179	1.50×10^{-2}	4.17×10^{-2}
Water	1000	1.27×10^{-3}	6.80×10^{-2}
Glicerol	1260	1.49×10^{-0}	6.34×10^{-2}

In the first few instants of the impact, liquid projects radially from beneath the droplet away from the impact point. This is caused by the rapid pressure increase in the liquid at the impact point. The numerical simulation accurately predicts this phenomenon. The variation of the shape of the droplet is well predicted throughout the impact/deformation, apart from minor discrepancies in the shape of the region between the radial projection and the upper surface of the droplet, where there is a slightly smoother transition in the numerical simulation than on the photographs.

Fig. 11(a) shows the time history of spread ratio of the impinging droplet (R^*) and thickness of the liquid layer over the surface (Th^*). The agreement between the numerical and experimental data is remarkably good. It is reasonable to assume that the numerical model gives a fairly accurate simulation of the process, since the shape and the dimensions of the liquid droplet outside the porous medium are predicted accurately.

In order to emphasize the differences between the impact of liquid droplets on permeable and non-permeable surfaces, Fig. 11(a) also shows the time history of the spread ratio (R^*) and the thickness of the liquid layer over the surface (Th^*) of a droplet impingement on a stainless steel surface. This configuration is similar to that for case 1, the only difference is the fact that the droplet is impinging on a non-permeable surface [41]. It is possible to note that the droplet impinging on a non-permeable surface presents a slightly larger spread ratio since the early stages of the impact. As pointed out by Chandra and Avedisian [41],

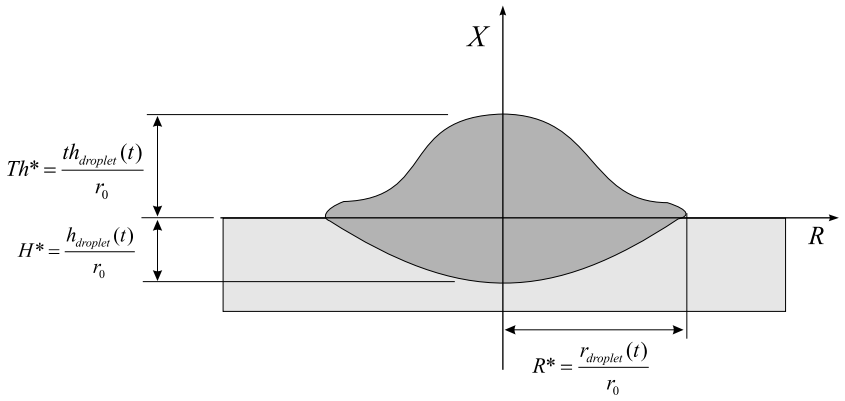

Fig. 9. Definition of the spread ratio (R^*), penetration depth (H^*) and thickness of the liquid layer outside the substrate (Th^*).

when a liquid droplet impinges on a flat solid non-permeable surface, there is a rapid increase in the pressure at the impact region, transforming the axial momentum of the liquid in a radial fluid flow, which causes the droplet to spread over the surface. However, for the impingement on permeable surfaces, the pressure increase is not so intense, since some liquid moves through the surface, despite the resistance imposed by the solid matrix of the porous substrate. In addition, capillary effects also draw the liquid into the substrate. As a result, lateral spreading is significantly reduced in relation to the impact on a non-permeable surface.

Many authors (among others [14,42,43]) reported that the droplet radius spreading over a porous surface increases as a function of t^n, where the value of n depends on the porous media and liquid droplet characteristics. The results obtained in the present work also indicate a tendency of increase in the drop radius as a function of t^n. The values of n obtained for the configurations described in Table 1 range from 0.155 to 0.5. These results are approximately similar to those reported by [42,43], which presented values of n ranging from 0.176 to 0.41.

Fig. 11(b) presents the time history of the liquid penetration depth for cases 1 and 6–9. As discussed in Section 1, previous modelling attempts to predict the rate of penetration of liquid into a porous medium ([42,43]) were derived from the Lucas–Washburn law, which does not account for inertial effects during the droplet impact. The Lucas–Washburn law is based on a t^n function, where a value of n is a constant equal to 0.5. It is possible to note in Fig. 11(b) that the impregnation curves resemble a straight line on the log-log graph, indicating a tendency related to a t^n function. Nevertheless, the value of n depends on the droplet and porous medium characteristics, similarly to the behaviour found for R^*. Furthermore, the shape of the impregnation curves presents some deviations from a t^n function. For instance, for cases 8 and 9 in Fig. 11(b), there are some discrepancies between the impregnation curves and a t^n function, while for the cases with smaller permeability (cases 1, 6 and 7) a t^n function is a good approximation. This fact may be related to the more intense momentum dissipation for the cases with smaller permeability. In fact, the momentum of the droplet plays a very important role in the dynamics of the process for the configurations tested.

Fig. 12 presents the time evolution of the shape of the impinging droplet obtained by numerical simulation for two configurations (cases 6 and 8), which represent similar DEM droplets impinging on concrete (case 6) and sand (case 8). The pore size for these configurations is considerably different, yielding to significant differences on the porous media permeability as shown in Table 1. A smaller value of permeability of the substrate yields to an increase on the drag term in the momentum equation (Eq. (13)), which is responsible for the resistance imposed to the fluid flow. The reduction of the permeability of the medium

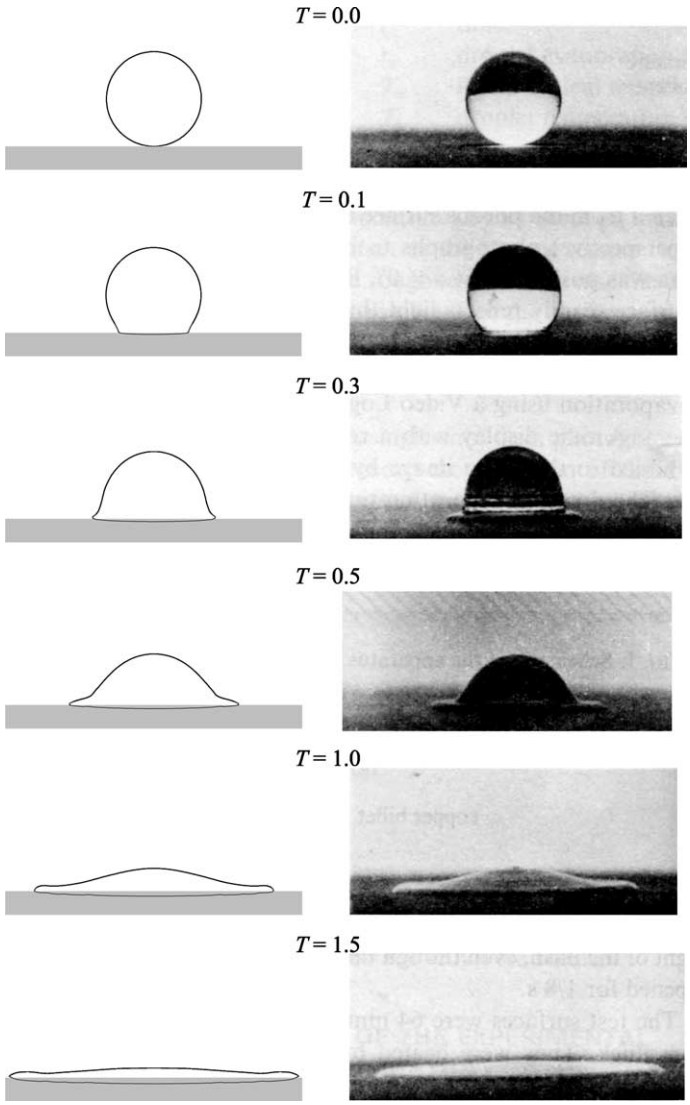

Fig. 10. Time evolution of the shape of the droplet: (left) numerical simulation vs. (right) experimental results [4].

considerably reduces liquid penetration, consequently increasing lateral spreading as the droplet is deformed outside the substrate. Accordingly, there is much more lateral spreading for case 6 (Fig. 12(a)) than for case 8 (Fig. 12(b)). The sequence of shapes displayed in Fig. 12(b) shows a much stronger absorption of the liquid by the substrate. The drag due to the substrate is not strong enough to rapidly reduce the initial droplet momentum. Furthermore, it presents relatively little resistance to the effects of capillary pressure in relation to case 8. In spite of the differences in the dynamics of the impact and absorption for the configurations tested, the final shapes obtained resemble a half-spheroid varying in penetration depth and spread ratio according to the value of permeability of the configurations tested.

In order to evaluate the model capability of accurately predicting the shape of the droplet inside the porous substrate, the results are compared with images of liquid droplets embedded in porous substrates

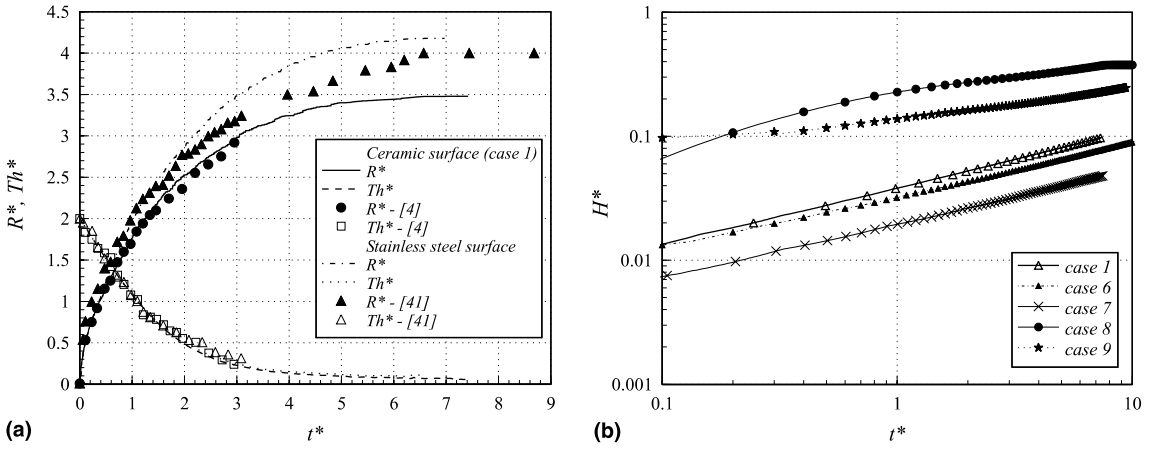

Fig. 11. Time history of (a) spread ratio of the impinging droplet (R^*) and non-dimensional thickness of the liquid layer over the surface (Th^*) for case 1 and (b) liquid penetration depth (H^*).

just after impact, obtained by Nuclear Magnetic Resonance [21]. By contrast with the experimental observations of Chandra and Avedisian [4], where the resistance imposed by the porous substrate was large enough to prevent significant liquid absorption, the conditions in the experiments reported by Reis [21] were such that the droplets were completely absorbed by the substrate (due to the high permeability of the substrates tested). Fig. 13 shows top view images of droplets embedded in the porous substrate after impingement, obtained in the NMR experiments. The images indicate that the assumption of an axi-symmetric representation of the droplet is valid, in spite of the small deviations of the droplet shape in relation to a perfect circle. As the droplet dimensions are relatively large compared to the particles and pores in the substrate, there is not a large amount of shape distortion due to capillary action such as was observed by Oliver et al. [44].

Fig. 14 shows comparisons of the shapes of the impinged droplet inside the porous substrate obtained by numerical simulation and NMR imaging. According to the numerical data and experimental observations, the droplet resides in the porous medium in a shape similar to a half-spheroid, whose aspect ratio depends on the porous medium and liquid droplet characteristics. There is a good agreement in the shape predicted for cases 10, 11 and 12 (a, b and c, respectively). However, the image obtained for case 12 displays clear signs that the solid particles composing the porous medium are disrupted during impact, which is not accounted for in the mathematical representation used in the numerical model. It can be seen that there is a distortion of the upper surface of the liquid region. In fact, a small crater is formed on the surface of the porous medium during the droplet impingement, and the structure visualised on the upper part of the droplet represents a section of this crater. The model failed to predict accurately the shape of the impinged droplet for case 13. The image shows that the impinged droplet on 50 μm glass beads produces more irregularities on the upper surface than the other configurations. Smaller particles are more easily displaced or dragged by the fluid flow, since the porous medium is unconsolidated. This causes a considerable discrepancy of the shape observed in relation to the numerical prediction.

Fundamentally, smaller glass beads result in smaller permeability values of the porous substrate, which should restrict the penetration of the liquid, causing it to spread more laterally (i.e. larger spread ratio). However, although the observed penetration depth is slightly smaller for 50 μm glass beads than for 120 μm glass beads (case 12), the spread ratio is not larger. This discrepancy may be related to the disruption of the upper surface of the shape of the droplet. The model is not able to predict this behaviour. Thus, the

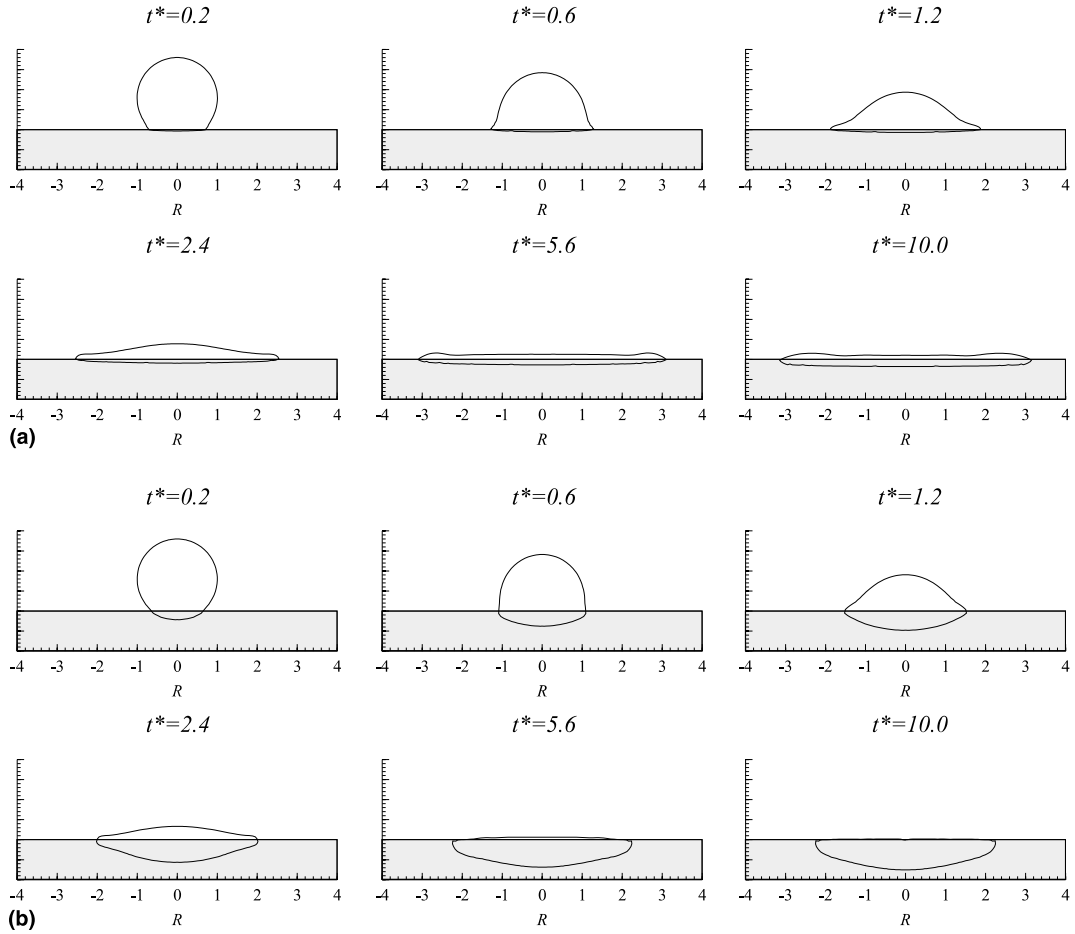

Fig. 12. Time evolution of the shape of the impinging droplet obtained by numerical simulation for (a) case 6 and (b) case 8.

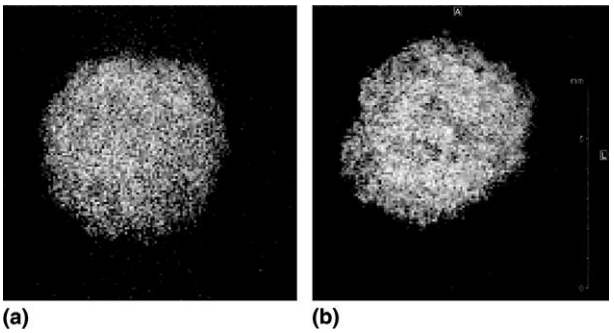

Fig. 13. Top view images of the impinged droplet: (a) water droplet impinging on 180 μm sand – case 10, (b) glycerol droplet impinging on 180 μm sand – case 11 [21].

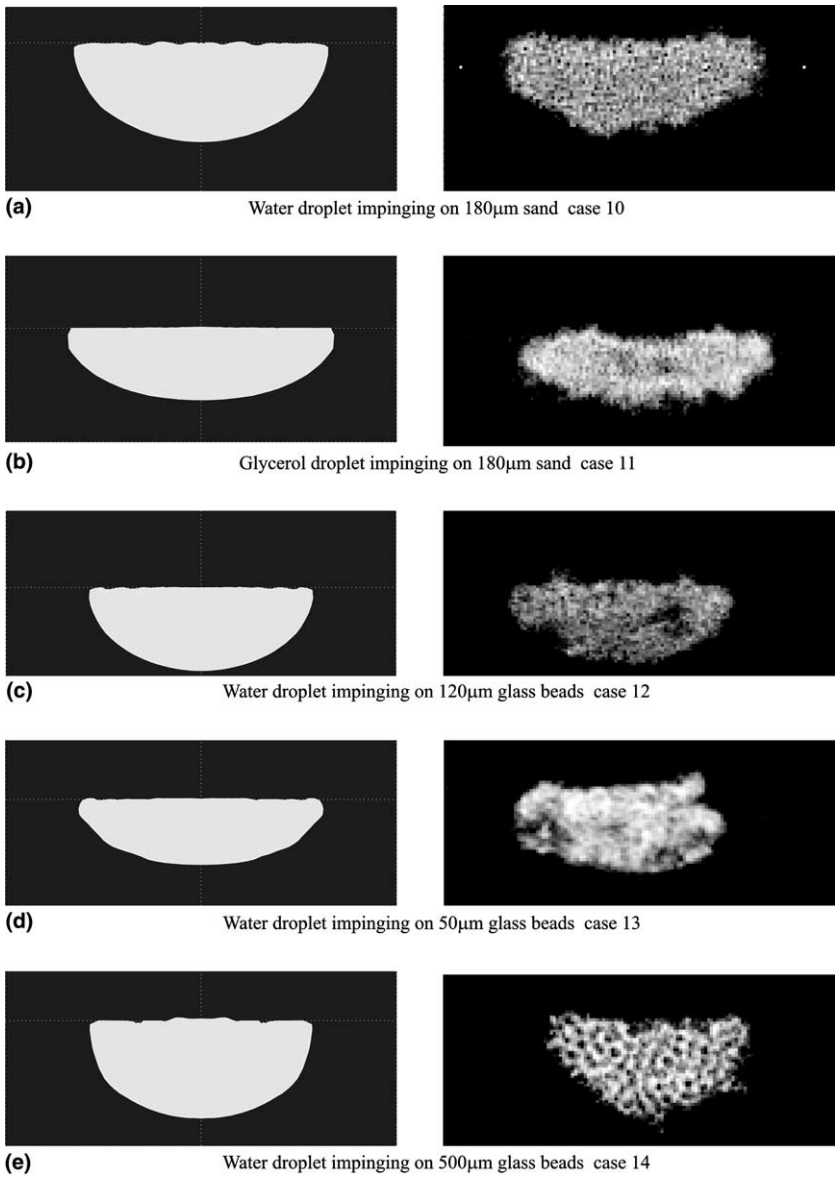

Fig. 14. Comparisons of the shapes of the impinged droplet inside the porous substrate obtained by numerical simulation (left) and (right) NMR imaging [21].

model not only overpredicts the reduction in penetration depth in relation to 120 μm glass beads, but it also overpredicts the spread ratio, mainly because it does not account for the disruption of the glass beads.

Although the shape of the impinged droplet is relatively well predicted for case 14, there are minor discrepancies in the penetration depth and spread ratio obtained. Penetration depth is slightly underpredicted, yielding an overprediction of the spread ratio.

Fig. 15 shows the comparison of the predicted spread ratio (R^*) after the droplet reaches its final shape obtained by numerical simulation and from experimental data. It can be seen that there is a reasonable agreement between the model predictions and experimental observations, except for cases 13 and 2.

As already stated, the poor predictions in case 13 can be attributed to disruption of the particles in the porous substrate; however, there is no obvious reason for the poor agreement found for case 2, though one can conjecture a probable explanation. Case 2 presents a larger free surface deformation, where the spread ratio is more than 5 and the thickness of the liquid film is reduced approximately 20 times in relation to its initial value. For configurations such as that, Fukai et al. [22] have pointed out that the utilisation of Eulerian formulations with a fixed grid for free surface flows may be questionable. They suggested that only a body-fitted co-ordinate system with a deformable mesh is able to fully capture the free surface dynamics, as the use of a fixed rectangular grid cannot represent with enough accuracy the normal and tangential stresses on the free surface.

Furthermore, as indicated in Fig. 15, although the results for droplet impingement on concrete (except case 2) are in close agreement with experimental data, the model has a tendency to slightly underpredict the spread ratio, which contributes to the poor agreement in case 2. This could indicate that either the representation of the transport inside the substrate is not as accurate for concrete as for other substrates, or that the concrete properties assumed in the simulations may not represent very accurately the substrates used by Roberts [19,20]. Roberts did not use a specific description of the concrete composition, but average values were taken from the literature within the range of variation of these properties. Roberts attributes the large standard deviation of the experimental data to differences between concrete ageing from one experimental site to the other, illustrating the importance of the adequate characterisation of the substrate.

In general the model is able to reproduce the variation of the spread ratio with the governing parameters. 57% of the data is within 10% agreement, and 79% of the data is within 15% agreement.

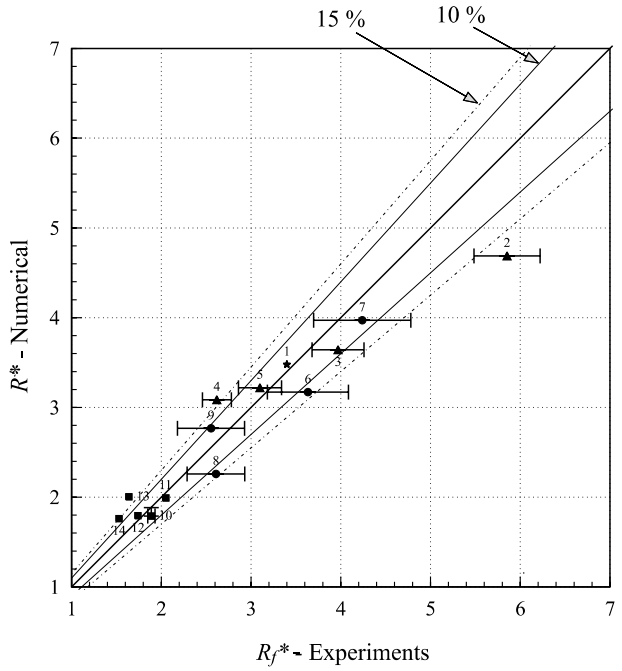

Fig. 15. Comparison of the predicted final spread ratio obtained by numerical simulation and experimental data (★ – [4], ● – [19], ▲ – [20], ■ – [21]).

5. Conclusions

A numerical model to simulate the impact/absorption of a liquid droplet on a porous medium has been developed. In order to accurately represent the dynamics of the fluid flow, surface tension effects inside and outside the porous medium were included in the model. In addition, special attention was given to the movement of the free surface inside the porous medium, and the link between the fluid flow outside and inside the porous medium, which ensures the requirement of momentum conservation across the porous medium interface. In order to verify the accuracy of the proposed computational model, its predictions have been compared with data from a number of experimental investigations. In general, the model gives results that show good agreement with the experimental data. The main deviations were found for droplets impinging on unconsolidated substrates with very small particles, where the impact of the liquid disrupts the loose particles, an effect not accounted for in the mathematical description.

References

[1] W. Cooper, F.H. Hardaway, L. Edwards, The evaporation of two thickened agent simulants from wet and dry concrete, Report No. CRDEC-TR-86033, CRDEC, Aberdeen Proving Ground, Aberdeen, MD, USA, 1986.
[2] W. Cooper, F.H. Hardaway, L. Edwards, The evaporation of two thickened agent simulants from wet and dry sand, Report No. CRDEC-TR-112, CRDEC, Aberdeen Proving Ground, Aberdeen, MD, USA, 1990.
[3] R.F. Griffiths, I.D. Roberts, Droplet evaporation from porous surfaces; model validation from field and wind tunnel experiments for sand and concrete, Atmos. Environ. 33 (21) (1999) 3531–3549.
[4] S. Chandra, Avedisian, Observation of droplet impingement on a ceramic porous surface, Int. J. Heat Mass Transfer 35 (1992) 2377–2388.
[5] N.C. Reis Jr., R.F. Griffiths, M.D. Mantle, L.F. Gladden, Investigation of the evaporation of embedded liquid droplets from porous surfaces using magnetic resonance imaging, Int. J. Heat Mass Transfer 46 (2003) 1279–1292.
[6] F.H. Harlow, J.P. Shannon, The splash of a liquid droplet, J. Appl. Phys. 38 (1967) 3855.
[7] K. Tsurutani, M. Yao, J. Senda, H. Fujimoto, Numerical analysis of the deformation process of a droplet impinging upon a wall, JSME Int. J. Series II 33 (1990).
[8] E.P. Ascoli, D.S. Dandy, L.G. Leal, Buoyancy-driven motion of a deformable drop toward a planar wall at low Reynolds number, J. Fluid Mech. 213 (1990) 287–311.
[9] C. Pozrikidis, The deformation of a liquid drop moving normal to a plane wall, J. Fluid Mech. 215 (1990) 331–363.
[10] M. Pasandideh-Fard, S. Chandra, J. Mostaghimi, A three-dimensional model of droplet impact and solidification, Int. J. Heat Mass Transfer 45 (2002) 2229–2242.
[11] J. Fukai, Z. Zhao, D. Poulikakos, C.M. Megaridis, O. Miyatake, Modelling of the deformation of a liquid droplet impinging upon a flat surface, Phys. Fluids A 5 (1993) 2588–2599.
[12] Z. Zhao, D. Poulikakos, J. Fukai, Heat transfer and fluid dynamics during the collision of a liquid droplet on a substrate – I. Modeling,, Int. J. Heat Mass Transfer 39 (13) (1996) 2771–2789.
[13] M. Bertagnolli, M. Marchese, G. Jacucci, I. St. Doltsinis, S. Noelting, Thermo-mechanical simulation of the splashing of ceramic droplets on rigid substrate, J. Comput. Phys. 133 (1997) 205.
[14] D. Danino, A. Marmur, Radial capillary penetration into paper: limited and unlimited liquid reservoirs, J. Colloid Interface Sci. 166 (1994) 245–250.
[15] A. Marmur, R.D. Cohen, Characterization of porous media by the kinetics of liquid penetration: the vertical capillaries model, J. Colloid Interface Sci. 189 (1997) 299–304.
[16] D. Seveno, V. Ledauphin, G. Martic, M. Vou, J. De Coninck, Spreading drop dynamics on porous surfaces, Langmuir 18 (2002) 7496–7502.
[17] V.S. Patankar, Numerical Heat Transfer and Fluid Flow, Hemisphere, Washington, DC, 1980.
[18] J.E. Welch, F.H. Harlow, J.P. Shannon, B.J. Daly, The MAC method – computing technique for solving viscous, compressible, transient fluid-flow problems involving free surfaces, Los Alamos Scientific Lab., Report No. LA3425, 1966.
[19] I.D. Roberts, Droplet evaporation from porous surfaces, Ph.D. Thesis, UMIST, 1995.
[20] R.F. Griffiths, I.D. Roberts, Droplet evaporation from porous surfaces; model validation from field and wind tunnel experiments for sand and concrete, Atmos. Environ. 33 (1999) 3531–3549 (see also I.D. Roberts, The evaporation of neat/thickened agent simulant droplets from porous surfaces, Final report on agreement No. 2044/013/CDBE, UMIST, 1996).
[21] N.C. Reis Jr., Droplet impingement and evaporation from porous surfaces, Ph.D. Thesis, UMIST, 2000.

[22] J. Fukai, Y. Shiiba, T. Yamamoto, O. Miyatake, D. Poulikakos, C.M. Megaridis, Z. Zhao, Wetting effects on the spreading of a liquid droplet colliding with a flat surface: experiments and modelling, Phys. Fluids 7 (1995) 236–247.
[23] L.E. Scriven, Dynamics of a fluid interface, Chem. Eng. Sci. 12 (1960) 98–108.
[24] P.G. Gennes, Wetting: statics and dynamics, Rev. Mod. Phys. 57 (part I) (1985) 827–863.
[25] V.E. Dussan, On the spreading of liquids on solid surfaces: static and dynamic contact lines, Annu. Rev. Fluid Mech. 11 (1979) 371–400.
[26] S. Whitaker, Advances in theory of the fluid motion in porous media, in: Flow Through Porous Media, American Chemical Society Publication, 1970.
[27] C.T. Hsu, P. Cheng, Thermal dispersion in a porous medium, Int. J. Heat Mass Transfer 33 (1990) 1587–1597.
[28] S. Ergun, Fluid flow through packed columns, Chem. Eng. Prog. 48 (1952) 89–94.
[29] A. Hadin, Forced convection in a porous channel with localised heat sources, J. Heat Transfer 116 (1994) 465–472.
[30] W.-S. Fu, H.-C. Huang, W.-L. Liou, Thermal enhancement in laminar channel flow with a porous block, Int. J. Heat Mass Transfer 39 (1996) 2165–2175.
[31] F.A.L. Dullien, Porous Media – Fluid Transport and Pore Structure, second ed., Academic Press, New York, 1992.
[32] B. Wang, W. Yu, A method for evaluation of heat and mass transport properties of moist porous media, Int. J. Heat Mass Transfer 31 (1988) 1005–1009.
[33] S.B. Nasrallah, P. Perre, Detailed study of a model of heat and mass transfer during convective drying of porous media, Int. J. Heat Mass Transfer 31 (1988) 957–967.
[34] N.C. Reis Jr., R.F. Griffiths, E.P.L. Roberts, finite volume method to solve free-surface fluid flow problems, in: M.J. Baines (Ed.), Numerical Methods on Computational Fluid Dynamics VI, Oxford, 1998, pp. 475–483.
[35] J.P. Van Doormal, G.D. Raithby, Enhancements of the SIMPLE method for predicting incompressible fluid flow, Numer. Heat Transfer 7 (1984) 147–163.
[36] B.D. Nichols, C.W. Hirt, R.S. Hotchkiss, SOLA-VOF: a solution algorithm for transient fluid flow with multiple free boundaries, Los Alamos Scientific Lab., Report No. LA-8355, 1980.
[37] B.J. Daly, W.E. Pracht, Numerical study of density-current surges, Phys. Fluids 11 (1968) 15–30.
[38] N.C. Reis Jr., Finite volume method to solve free-surface fluid flow problems, M.Phil. Thesis, UMIST, 1997.
[39] I. Odler, H. Koster, Investigations on the structure of fully hydrated Portland cement and tricalcium silicate pastes. II. Total porosity and pore size distribution, Cement Concrete Res. 16 (1986) 893–901.
[40] S. Kelham, A water absorption test for concrete, Mag. Concrete Res. 40 (1988) 106–110.
[41] S. Chandra, C.T. Avedisian, On the collision of a droplet with a solid surface, Proc. Roy. Soc. Lond. A 432 (1991) 13–41.
[42] M. Denesuk, G.L. Smith, B.J.J. Zelinski, N.J. Kreidl, D.R. Uhlmann, Capillary penetration of liquid droplets into porous materials, J. Colloid Interface Sci. 158 (1993) 114–120.
[43] R.K. Holman, M.J. Cima, S.A. Uhland, E. Sachs, Spreading and infiltration of inkjet-printed polymer solution droplets on a porous substrate, J. Colloid Interface Sci. 249 (2002) 432–440.
[44] J.F. Oliver, L. Agbezuge, K. Woodcock, A diffusion approach for modelling penetration of aqueous liquids into paper, Colloids Surf. A 89 (1994) 213–226.